Structure Stabilization by Mixed Anions in Oxyfluoride Cathodes for High-Energy Lithium Batteries

Sung-Wook Kim,[†,‡] Nathalie Pereira,[§] Natasha A. Chernova,[∥] Fredrick Omenya,[∥] Peng Gao,[†] M. Stanley Whittingham,[∥] Glenn G. Amatucci,[§] Dong Su,[*,†] and Feng Wang[*,†]

[†]Brookhaven National Laboratory, Upton, New York 11973, United States, [‡]Nuclear Fuel Cycle Process Development Group, Korea Atomic Energy Research Institute, Daejeon 34057, Republic of Korea, [§]Department of Materials Science and Engineering, Rutgers University, North Brunswick, New Jersey 08902, United States, and [∥]Institute for Materials Research and Department of Chemistry, State University of New York at Binghamton, Binghamton, New York 13902, United States

ABSTRACT Mixed-anion oxyfluorides (*i.e.*, FeO_xF_{2-x}) are an appealing alternative to pure fluorides as high-capacity cathodes in lithium batteries, with enhanced cyclability *via* oxygen substitution. However, it is still unclear how the mixed anions impact the local phase transformation and structural stability of oxyfluorides during cycling due to the complexity of electrochemical reactions, involving both lithium intercalation and conversion. Herein, we investigated the local chemical and structural ordering in $FeO_{0.7}F_{1.3}$ at length scales spanning from single particles to the bulk electrode, *via* a combination of electron spectrum-imaging, magnetization, electrochemistry, and synchrotron X-ray measurements. The $FeO_{0.7}F_{1.3}$ nanoparticles retain a FeF_2-like rutile structure but chemically heterogeneous, with an F-rich core covered by thin O-rich shell. Upon lithiation the O-rich rutile phase is transformed into Li—Fe—O(—F) rocksalt that has high lattice coherency with converted metallic Fe, a feature that may facilitate the local electronic and ionic transport. The O-rich rocksalt is highly stable over lithiation/delithiation and thus advantageous to maintain the integrity of the particle, and due to its predominant distribution on the surface, it is expected to prevent the catalytic interaction of Fe with electrolyte. Our findings of the structural origin of cycling stability in oxyfluorides may provide insights into developing viable high-energy electrodes for lithium batteries.

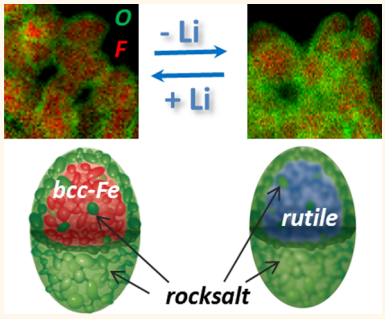

KEYWORDS: lithium batteries · mixed-anion cathodes · iron oxyfluoride · scanning transmission electron microscopy (STEM) · electron energy loss spectroscopy (EELS)

The demand for high-energy storage systems is increasing rapidly, especially for large-scale applications in electric vehicles. Today's lithium-ion batteries utilize graphite for the anode, with a specific capacity of 372 mAh g^{-1}, while the capacity of the commercially available cathodes (even those most advanced ones, *i.e.*, $LiMn_2O_4$, $LiFePO_4$, $LiNi_{1/3}Mn_{1/3}Co_{1/3}O_2$) is low, ~120−180 mAh g^{-1}; hence, the capacity of the current cathodes is the bottleneck for the development of low-cost batteries for vehicle application. To expand the search of new cathode materials beyond traditional constrains in designing cathodes (with open framework and Li-containing requirements), Li-free conversion materials started to be considered, in particular those transition metal compounds, based on the chemistry: $M^{(n+)}X_z + nLi^+ + ne^- = Li_nX_z + M^0$ (M = transition metals). They are promising for next-generation lithium batteries due to the exceptionally high specific-capacity (~500−700 mAh g^{-1}; 2- to 4-fold higher than that of conventional intercalation compounds).[1−4] There are various types of conversion compounds, including the metal oxides, nitrides, sulfides, and fluorides.[3,4] However, the reaction potentials scale with the electronegativity of anions, spanning a wide range, and only metal fluorides have sufficiently high working potentials for use as cathodes.[1,5−11] However, their poor cycling stability and low energy efficiency (arising from large voltage hysteresis) remain a formidable hurdle to their practical applications.

Cycling performance in metal fluorides is predominantly affected by cation species, as being demonstrated by reasonable reversibility in FeF_2 *vs* irreversibility in CuF_2.[7,11] Interestingly, some reversibility in $Cu^{2+/0}$ redox was achieved in mixed-cation fluorides,

* Address correspondence to fwang@bnl.gov, dsu@bnl.gov.

Received for review June 16, 2015 and accepted August 22, 2015.

Published online August 24, 2015
10.1021/acsnano.5b03643

$Cu_yFe_{1-y}F_2$ in the form of solid solution, so highlighting one new way of tailoring the electrochemical performances of conversion electrodes.[7,11,12] Similarly, the incorporation of mixed anions to form a solid solution was proved to be a viable approach to tuning the electrochemical properties of conversion compounds.[13−20] For instance, O-substituted FeO_xF_{2-x} ($0 \leq x \leq 1$) exhibits excellent capacity retention under prolonged cycling, while a recent electrochemical study also revealed a reduced voltage hysteresis upon cycling, leading to the improved energy efficiency of the mixed-anion system.[13,18] In addition, FeO_xF_{2-x} is expected to deliver more energy than pure FeF_2 due to the higher oxidation state of Fe (with incorporation of O) and improved electronic conductivity.[13,15]

Recent experimental and theoretical studies confirmed that, in this mixed-anion system, the lithium reaction involves both intercalation and conversion *via* a complex dynamical process, leading to a nanocomposite of metallic Fe^0, LiF, and rocksalt Li−Fe−O(−F).[13−20] The nanocomposite is reconverted to F-rich rutile and O-rich rocksalt after charge, instead of recovering its initial rutile phase.[17] In those previous experimental studies, bulk techniques, such as X-ray and nuclear magnetic resonance (NMR), can only provide averaged information with data collected from large areas of agglomerates. Moreover, X-ray scattering techniques are mostly sensitive to Fe-based phases, but they are incapable of detecting the light constituents (*i.e.*, LiF and Li_2O) due to the small X-ray scattering power of light elements, and they do not have sufficient resolution to probe the local, heterogeneous electrochemical reactions within individual nanoparticles. It remains unclear how those phases are spatially distributed and how they evolve with cycling and thereby affect the cycling stability of the FeO_xF_{2-x} electrode.

Scanning transmission electron microscopy (STEM), coupled with electron energy-loss spectroscopy (EELS), has been proven powerful in identifying the structural and chemical ordering in electrode materials due to its extraordinary spatial resolution (down to atomic level) and high sensitivity to the chemical states of both light elements (*i.e.*, Li) and transition metals in the constituents.[7,8] Here, we report the detailed investigation of the chemical and structural orderings in $FeO_{0.7}F_{1.3}$ *via* STEM-EELS, combined with complementary magnetization measurements, synchrotron X-ray diffraction (XRD), and X-ray absorption spectroscopy (XAS). Spatial distribution of all constituent elements (*i.e.*, Li, Fe, O, F) and valence states of Fe at pristine and (de)lithiated states were resolved at the subnanometer scale. Magnetic analysis was carried out to investigate the evolution of the Fe-containing magnetic species in the bulk electrodes.[7,21−23] Local reordering was found to occur in the structure and chemical species within individual nanoparticles upon lithiation/delithiation, forming a heterogeneous core−shell structure, a feature that may be critical for the long-term cycling stability in O-substituted oxyfluorides.

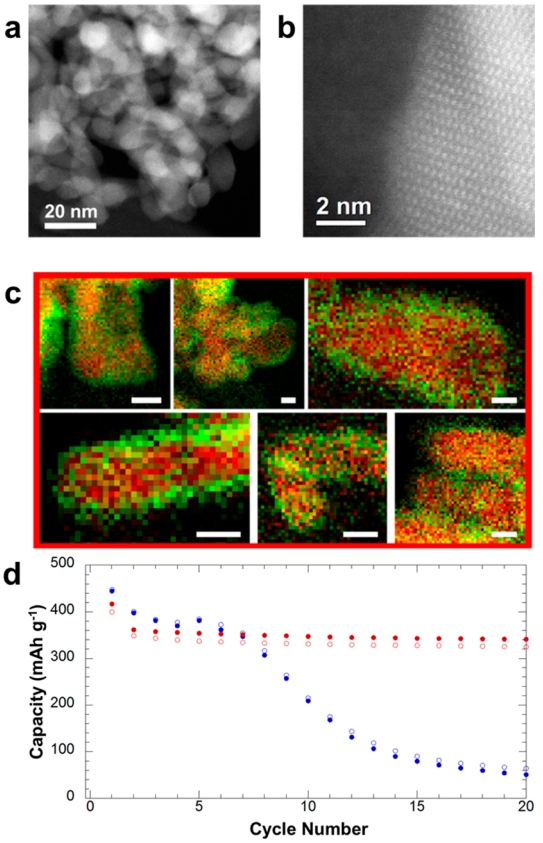

Figure 1. Local structural and chemical ordering of as-synthesized $FeO_{0.7}F_{1.3}$ nanoparticles: (a) low-magnification ADF image of multiple particles, (b) high-resolution ADF lattice image, and (c) STEM-EELS spectrum-images for the elemental distribution of O (green) and F (red) from many locations (scale bar: 5 nm), (d) electrochemical cycling of $FeO_{0.7}F_{1.3}$ (red) in comparison to that of FeF_2 (blue).

RESULTS AND DISCUSSION

EELS Imaging for Resolving O/F Distribution within Single $FeO_{0.7}F_{1.3}$ Particles. Despite rapid advances in electron microscopy/spectroscopy techniques, their application in probing light elements with high spatial resolution and chemical sensitivity has been a great challenge due to the low scattering power. This is the case particularly in studying insulating fluorides where the radiolysis damage becomes a big concern (see details in Supporting Information, S1).[24,25] To visualize chemical inhomogeneity across single $FeO_{0.7}F_{1.3}$ particles of only about 10 nm (in the short dimension), we developed an EELS-based spectrum-imaging technique, using the intensity ratio between O and F K-edges to differentiate these two neighboring elements. As shown in Figure 1, with an optimization of the conditions (provided in Supporting Information, S1) to reduce the dose rate and accumulated dose, we were able to identify the spatial distribution of O/F in individual particles.

Core–Shell Structure of Pristine $FeO_{0.7}F_{1.3}$. The as-synthesized particles have a well-defined ellipsoidal shape, about 10–15 nm wide, 30–50 nm long (Figure 1a). The single-crystalline nature of the nanoparticles was identified by high-resolution STEM imaging (Figure 1b and Supporting Information, Figure S2a). $FeO_{0.7}F_{1.3}$ has a rutile structure, basically same as FeF_2, while the Fe valence was changed to a value between 2+ and 3+ (Supporting Information, Figure S2b–d) due to O substitution. And a nonuniform distribution of O and F was revealed by high-resolution elemental mapping, typically forming an O-rich shell and F-rich core in individual particles (Figure 1c; Supporting Information, Figure S3 for corresponding ADF images).

This core–shell structure was commonly observed in $FeO_{0.7}F_{1.3}$ nanoparticles and the thickness of the O-rich shell varies from particle to particle, in the range of 0.5–3.0 nm. The elemental separation between O and F in a single particle suggests that the substitution of F by O is not homogeneous, but preferentially takes place in the near-surface region, possibly due to the limited diffusion distance of O into FeF_2, or the high thermodynamic stability of the core–shell structure. Despite the nonuniform distribution, F and O are present across the entire particles, and thus, it is speculated that no pure oxides (*e.g.*, Fe_2O_3, Fe_3O_4) or pure fluorides (*e.g.*, FeF_2, FeF_3) exist (Supporting Information, Figure S4a–c). Oxygen substitution occurs throughout the entire particle although there exists an oxygen gradient with less oxygen in the core than that in the surface. Therefore, we expect an improvement in electronic conductivity of the entire material (due to the change in the electronic structure).[15]

Figure 1d shows the cycling data of $FeO_{0.7}F_{1.3}$ compared to that of the pure FeF_2, demonstrating a significant improvement of electrochemical cycling stability in the material with O substitution. But due to the complexity of electrochemical reactions (involving both intercalation and conversation) and the high chemical heterogeneity across single particles, detailed studies at single-particle level are needed in order to understand how O substitution affects the morphological and structural changes in $FeO_{0.7}F_{1.3}$ upon (de)lithiation.

Reversible Morphological Evolution. Figure 2 shows the typical voltage profile and representative STEM-ADF images showing the morphology of the $FeO_{0.7}F_{1.3}$ particles at various lithiated and delithiated states in the first cycle. There is no noticeable morphological change of particles in the early stage of lithiation, *i.e.*, in the sloping region above 2.0 V, where intercalation mainly occurs (Figure 2b,c).[13] But, with further lithiation (in the long plateau region at about 1.5 V), nanosized segregates are formed as a result of the conversion reaction (Figure 2d,e). Those segregates are metallic Fe^0 and/or rocksalt Li–Fe–O(–F) but become

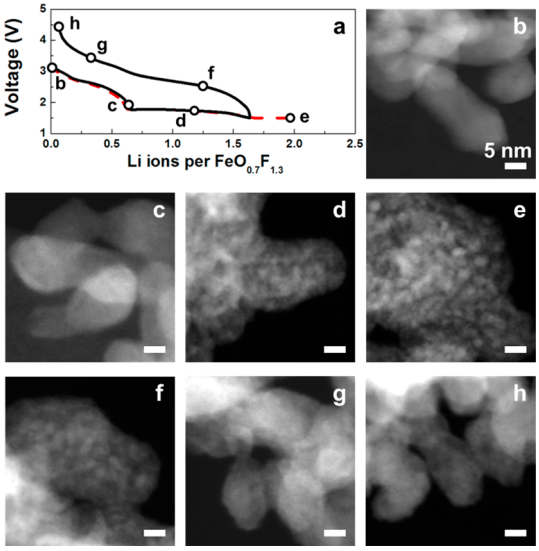

Figure 2. Morphological evolution of $FeO_{0.7}F_{1.3}$ nanoparticles during the first electrochemical cycle: (a) voltage profile, and (b–h) corresponding ADF images recorded from the samples at different (de)lithiated states (as indicated in Figure 2a).

highly disordered, which was identified by electron diffraction measurements (see Supporting Information, Figure S5). The nanocomposite is then reconverted to the disordered rutile and rocksalt phases after charge, instead of recovering its initial high-crystalline rutile phase. The results are consistent with previous reports.[13,17,20] Surprisingly, the initial morphology of the particles is largely recovered after charging (Figure 2f–h), despite the complex phase separation and recombination during cycling.[13,17,20] The stable particle morphology, without pulverization or breakdown of particles, which appears to be inherent to FeO_xF_{2-x}, may be largely attributed to the structural/chemical ordering within the particles (as discussed below).

Evolution of Magnetic Properties. The study of reversible behavior at single-particle level was complemented by investigation of the magnetic properties of bulk electrodes during the first cycle (Figure 3). Two series of samples (first tape, and second tape) were studied to ensure the reproducibility of our data. For each sample, magnetization measurements were performed at 2 K (Supporting Information, Figure S6). Figure 3a shows the measured values of saturation magnetization, obtained by linear extrapolation of high-field magnetization to a zero-field, at various (de)lithiated states. There is a clear change of trend in magnetization at the end of the intercalation process, from slow increase to a fast increase, which is associated with the formation of metallic Fe^0, as revealed by ADF imaging (Figure 2).

The small rise in magnetization upon initial intercalation may be due to the reduction of Fe^{3+} to Fe^{2+}, suggesting a more ferrimagnetic character of the Fe^{2+} compound. Upon charge, magnetization decreases

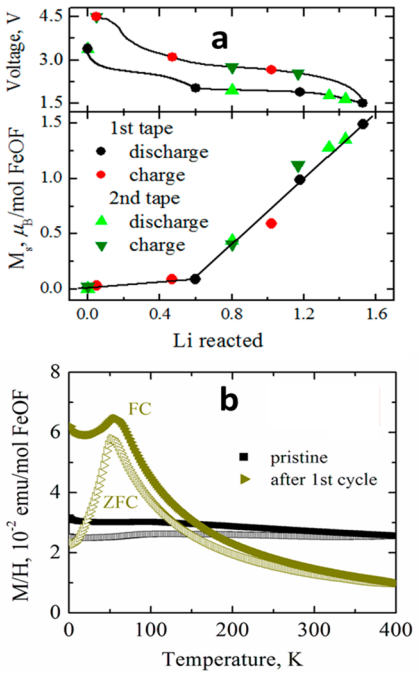

Figure 3. Evolution of the magnetic properties of the $FeO_{0.7}F_{1.3}$ electrodes as a function of the states of charge during the first electrochemical cycle: (a) voltage profile showing the states of discharge and charge probed by the magnetization measurements, and corresponding values of saturation magnetization at 2 K and (b) temperature dependence of the field-cooled (FC; solid symbols) and zero-field cooled (ZFC; open symbols) magnetic susceptibilities of the electrodes at the pristine state and after the first cycle.

rapidly, as metallic Fe^0 is consumed, while toward the end of the charge process, a slow decrease of magnetization becomes observable. Notably, the magnetization dependences follow the same trend upon discharge and charge, indicating much better reversibility of this system compared to FeF_2.[7] The saturation magnetization achieved upon discharge to 1.5 V is 1.5 μ_B mol^{-1}, *i.e.*, lower than the 2.2 μ_B mol^{-1} expected for metallic Fe^0, but comparable to the reported value of the lithiated FeF_2.[7,26]

Interestingly, the measurements of field-cooled- and zero-field-cooled magnetic susceptibility (Figure 3b and Supporting Information, Figure S7) reveal subtle differences in the magnetic properties between the cycled $FeO_{0.7}F_{1.3}$ electrodes and the pristine ones, despite the similarity in their saturated magnetization (M/H). The temperature dependence of the magnetic susceptibility of the cycled material overall resembles that of the rutile FeF_2 phase, except that the antiferromagnetic transition temperature is downshifted to 47 K, compared to 78.3 K observed for FeF_2.[7] Such a change in the magnetic properties should be attributed to the local structural and chemical reorganization revealed by STEM-EELS during the first cycle (as discussed below).

Local Chemical Evolution. In addition to the morphological evolution revealed by annual-dark-field

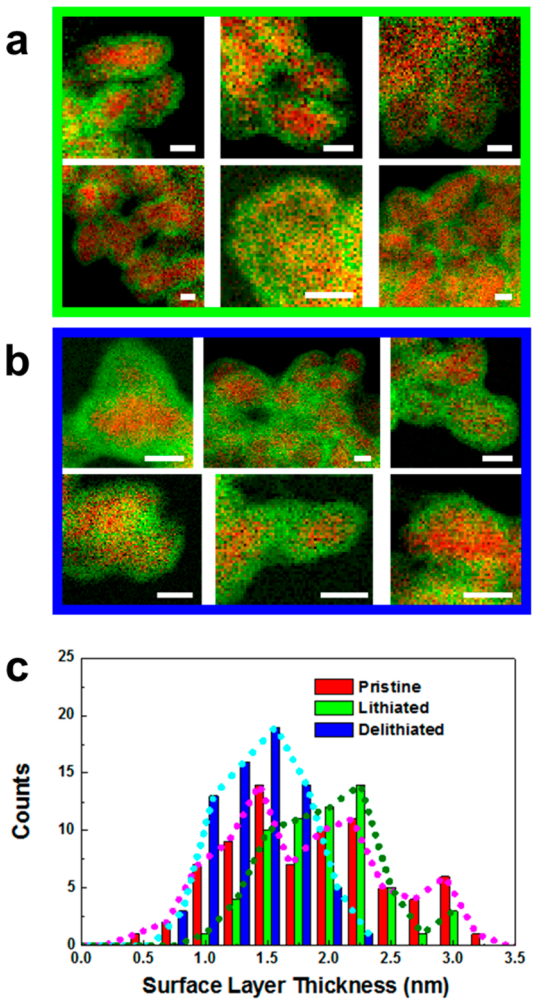

Figure 4. Retention of core−shell structure during the first cycle shown by the elemental distribution of O (green) and F (red) in individual $FeO_{0.7}F_{1.3}$ particles at (a and b) lithiated, delithiated states, and (c) the thickness of the O-rich shells (scale bar: 5 nm).

(ADF)-STEM imaging (Figure 2), information on local chemical redistribution due to the lithiation and delithiation processes was obtained by STEM-EELS spectrum-images recorded from many different particles as shown in Figure 4 (see also Supporting Information, Figures S8 and S9). The core−shell structure (shown in Figure 1c) is sustained after (de)lithiation (Figure 4a,b). Both O and F signals were observed across the particles (Supporting Information, Figure S4d−i), similar to the pristine sample. The retention of the original core−shell structure suggests the limited diffusion distance of O and F during cycling. We also measured the thickness of O-rich layer from tens of particles, and the results are depicted in the form of histogram in Figure 4c in comparison to that from the pristine $FeO_{0.7}F_{1.3}$ (as given in Figure 1c). With lithiation, the thickness of O-rich shell increases slightly to 1.0−3.0 nm, likely due to the volume expansion of the shell where lithium was incorporated to form lithiated surface phase (to be discussed below). After one cycle

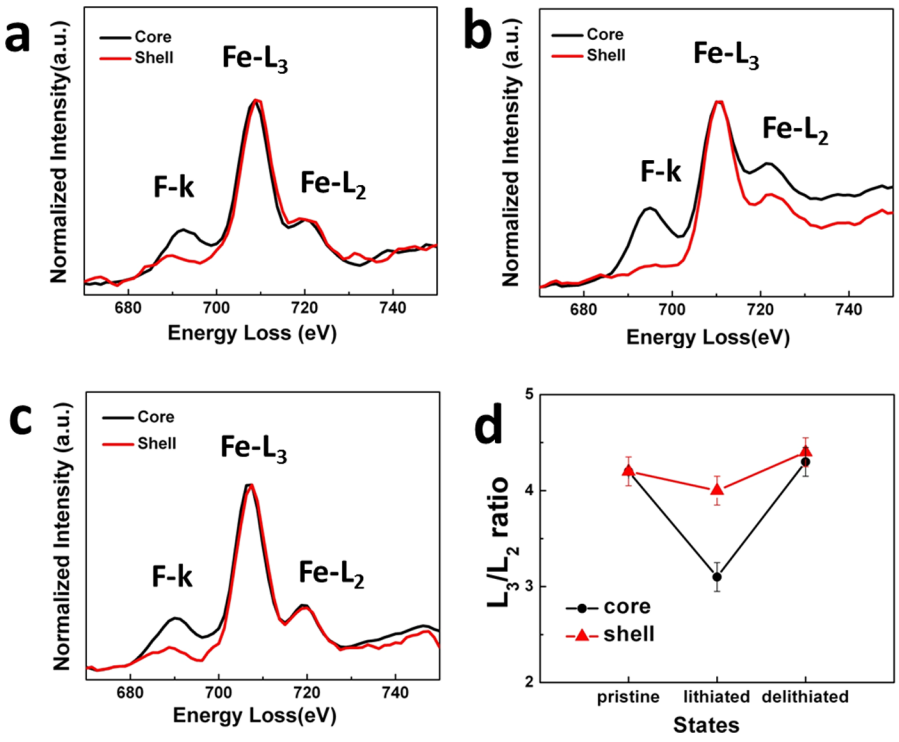

Figure 5. EELS spectra of Fe $L_{2,3}$ edges recorded from the core (black) and shell (red) regions of $FeO_{0.7}F_{1.3}$ particles, at (a) pristine, (b) lithiated, and (c) delithiated states and (d) corresponding Fe−L_3/L_2 ratio (see Figure S10 for data analysis).

it becomes 0.7−2.2 nm, as a result of delithiation, which is comparable to those of the pristine samples.

On the other hand, the redox of Fe is expected to vary across single particles due to heterogeneity in the chemical distribution (O/F ratio), *i.e.*, the existence of a core−shell structure. Therefore, STEM-EELS was used to track the valence change of Fe from the spectrum images in both the shell and the core regions in Figure 5a−c and Supporting Information, Figure S10.[19,20,27−29] The lithiated one had distinguishable spectra at the core and the shell, implying the different redox behaviors at the two regions. It can be clearly seen that the spectra at the core changed significantly after lithiation and then recovered after delithiation (Supporting Information, Figure S10a), indicating the reversible redox reaction of Fe at the F-rich core. In contrast, there is no remarkable change in the spectra recorded from the shell (Supporting Information, Figure S10b). To clearly show the change in valence of Fe at various states, the ratios of L_3/L_2 were extracted quantitatively using the Gaussian fitting method (after background subtraction) and given in Figure 5d (see also details of data analysis in Supporting Information, S10). The significant change in L_3/L_2 ratio at the core, in contrast to the small change at the shell (within the range of error), again shows the preferential electrochemical reaction at the F-rich core.

Bulk measurements at electrode level, by X-ray pair-distribution function (PDF) and NMR, showed similar results, namely, transformation of rutile FeO_xF_{2-x} to LiF, Fe^0, and rocksalt Li−Fe−O(-F) upon lithiation, and then reconversion into highly disordered F-rich rutile and rocksalt phases upon delithiation, which was also confirmed by electron-diffraction studies (see Supporting Information, Figure S5).[17] The phase separation of F-rich rutile and O-rich rocksalt, as confirmed by PDF-NMR study, is further confirmed by the observation of chemical separation the F-rich core and the O-rich shell. However, only through local STEM-EELS analysis were we able to confirm that the major Fe species contained in the O-rich shell are electrochemically inactive at voltages above 1.5 V, and the dominant redox reaction occurred at the core region (with transitions between Fe^0/LiF mixed phase a the F-rich rutile phase).

Local Structural Ordering. Lattice coherence was previously reported in Fe^0 nanocrystallites converted from FeF_2 and FeF_3.[7,29] To understand how this fascinating phenomenon was affected by O substitution, lattice images were taken from fully lithiated $FeO_{0.7}F_{1.3}$ samples (Figure 6). As shown in Figure 6a, there appears to be multiple fine crystallites, but interestingly, the corresponding fast Fourier transformation (FFT) image of the whole area (inset of Figure 6a) shows a highly periodic pattern (consistent to the projection of [111] zone axis of BCC-Fe^0), instead of the ring-like patterns (that are characteristic of randomly oriented crystallites). The FFT patterns for those individual crystallites, displayed in Figure 6b−e, reveal that the structure of these crystallites, either metallic Fe^0 or the rocksalt phase Li−Fe−O(−F), are not identical, but

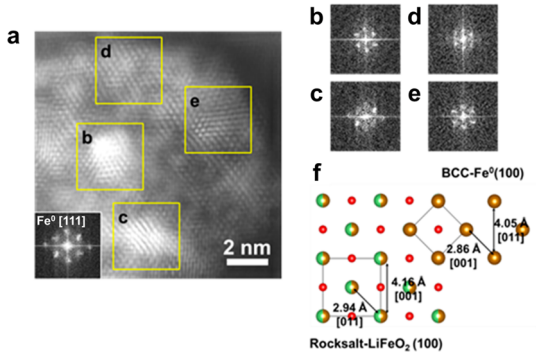

Figure 6. Structural ordering in the fully lithiated $FeO_{0.7}F_{1.3}$: (a) high-resolution ADF lattice image (inset, FFT pattern obtained from whole area), and (b−e) FFT patterns obtained from local regions as indicated by squares in (a). (f) Atomic arrangement of rocksalt $LiFeO_2$ and BCC-Fe^0 in the (100) plane (yellow, Fe; green, Li; red, O).

their crystallographic orientations are coherent. The lattice coherency of crystallites converted from the same $FeO_{0.7}F_{1.3}$ particle is commonly observed in many different locations in the fully lithiated electrodes (Supporting Information, Figure S11). The concentration of Fe^0 in the converted FeO_xF_{2-x} is obviously lower than that in FeF_2 and in return, percolated network appears to be formed with Fe^0 fine crystallites and rocksalt Li−Fe−O(−F) phase, as demonstrated by the lattice coherency and interconnection between the two.

In the lithiated FeF_2 and FeF_3, the interconnected Fe^0 is the only measurable crystalline phase.[7,8,30] However, in the lithiated $FeO_{0.7}F_{1.3}$, metallic Fe^0 (with the body-center cubic; BCC structure) and the rocksalt Li−Fe−O(−F) coexist inside individual particles.[17] Therefore, it would be interesting to explore how the two phases with different structures interface coherently. Since detailed crystallographic information for rocksalt Li−Fe−O(−F) is not available, the structure of $LiFeO_2$ (PDF#17-0938) is simply taken by assuming that they have similar lattice parameters and atomic configurations. The crystal structures of the BCC-Fe^0 phase (PDF#06-0696) and the rocksalt $LiFeO_2$ are illustrated in the Supporting Information, Figure S12. Their lattice distances and bonding angles are comparable in the (100) plane of the two phases (difference <3%). In addition, the [001] direction of Fe^0 and the [011] of $LiFeO_2$ are well matched. Hence, the two phases may tend to share the interface coherently to reduce interfacial energy. The model of the atomic arrangement of Fe along the (100) plane in the two phases is illustrated in Figure 6f. The same atomic models are shown in Figure S13 along [111] of the BCC-Fe^0 phase (blue) (being also equivalent to the [110] of the rocksalt $LiFeO_2$ (yellow)). The atomic arrangement is consistent with the high-resolution ADF-STEM image in Figure 6a, affording evidence of coherency among the particles of these two different phases.

The local TEM studies were also complemented by temperature dependent AC susceptibility measurements,

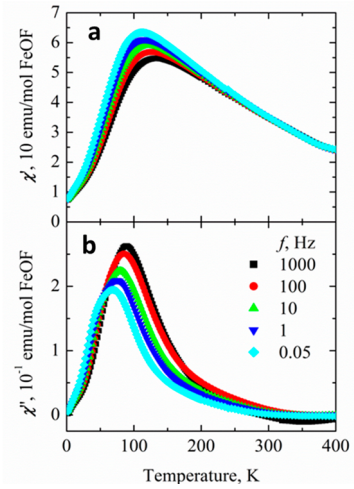

Figure 7. Determination of the size of the magnetic domains in the fully lithiated electrodes by temperature dependence of real (a) and imaginary (b) components of AC susceptibility, measured at various frequencies.

wherein, the size of the magnetic domains in the fully lithiated electrodes (discharged to 1.5 V) was estimated using a similar procedure as we employed in studying FeF_2.[7] Figure 7 gives both the real- and the imaginary-components of the susceptibility, revealing the pronounced maxima between 65 and 130 K, which shifts toward lower temperatures with the decrease of AC field frequency. The relative shift per decade of frequency expressed as $\Delta T_b/T_b\Delta(\log(\omega)) \cong 0.07$ (T_b is the blocking temperature and $\omega = 2\pi f$ is the angular frequency) is typical of superparamagnetic particles. Thus, we have attributed the low-temperature maxima of the ZFC curves to the formation of superparamagnetic Fe particles and we used the relationship between the blocking temperature T_b and the particle volume V, $T_b = KV/25k_B$ (K is the magnetocrystalline energy and $k_B = 1.38 \times 10^{-16}$ erg K^{-1} is the Boltzmann constant), to estimate the particle size based on magnetic susceptibility. Assuming the magnetocrystalline constant $K = 4.8 \times 10^5$ erg cm^{-3} of metallic Fe^0, and spherical particle shape, it came to a conclusion that the particle diameter varies from 9 nm at the end of the intercalation process to 11 nm at the end of discharge to 1.5 V, and this change is reversible upon charge. The results from magnetic measurements imply a larger sized particle than that measured by TEM (2−3 nm), which indicates that, similar to the FeF_2 case, the particles in the lithiated $FeO_{0.7}F_{1.3}$ are not isolated but are interconnected.[7] However, the lithiation process in $FeO_{0.7}F_{1.3}$ is more complicated, involving the formation of metastable intercalated phase, which is subsequently decomposed into an O-rich rocksalt phase and LiF, even before the conversion to the Fe^0, rocksalt Li−Fe−O(−F), and LiF occurs.[16] The Li−Fe−O(−F) phase is expected to be magnetic; thus, the superparamagnetic particles may be composed of

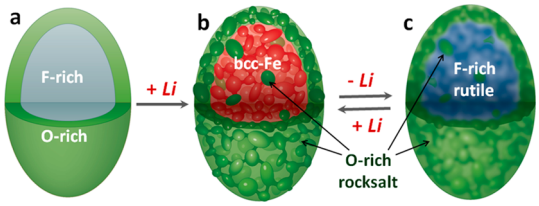

Figure 8. Schematic illustration of structural/chemical ordering of $FeO_{0.7}F_{1.3}$ at (a) pristine rutile, F-rich at the core and O-rich at the shell; (b) lithiated state, bcc-Fe^0 (core) and O-rich rocksalt predominately at the shell; and (c) delithiated state, F-rich rutile (core), and O-rich rocksalt predominately at the shell.

magnetically interacting rocksalt and metallic Fe^0 phases. A recent study based on small-angle X-ray scattering and the pair-distribution function measurements suggested that metallic Fe^0 particles converted from FeO_xF_{2-x} are about 2−3 nm, which is consistent with our TEM observation, but does not support the formation of a percolated network.[11] This may be explained by the coexisting rocksalt phase between the Fe^0 nanoparticles (as being observed by TEM).

Therefore, a combination of the local lattice imaging (within single particles) with the bulk magnetization measurements (at electrode level) provides direct evidence of the formation of a percolated network of Li−Fe−O(−F) rocksalt and metallic Fe^0, interwoven spatially with high lattice coherency. This development will facilitate the electronic and ionic transport required for delithiation, which eventually turns them into new rutile and rocksalt phases, at the core and shell, respectively. The observation is consistent with the recent report.[18]

Impact of O-Substitution on Electrochemical Cycling Stability. Figure 8 shows a schematic illustration of the morphological and chemical evolution in a single $FeO_{0.7}F_{1.3}$ particle. The $FeO_{0.7}F_{1.3}$ particle, being initially single-crystalline and encapsulated by thin O-rich shell in the pristine state, was turned into a nanocomposite upon lithiation, with metallic Fe^0 crystallites and rocksalt Li−Fe−O(−F), the latter being highly concentrated in the surface layer. This reorganization may be beneficial to long cycling stability of $FeO_{0.7}F_{1.3}$, by reducing the catalytic interaction of nanosized metallic particles (*i.e.*, Fe^0) with the electrolyte, which is believed to be the main reason underlying the decomposition of the electrolyte on the particle's surface.[31] Further, after one cycle, the overall morphology and core−shell structure of F-rich rutile core and O-rich rocksalt shell are maintained (although the two phases became highly disordered). Consequently, the F-rich core dominantly participates in the electrochemical reaction, while the O-rich shell is relatively stable upon cycling to sustain the particle integrity (as revealed in Figure 2). One important feature of the core−shell structure in FeO_xF_{2-x} is the lattice coherency of the core and shell, ensuring the integrity of the whole particle. This is distinctly different from the surface oxidized FeF_3 or fluorinated Fe_3O_4 (or Fe_2O_3) where a simple mixture of iron oxides/fluorides nanocomposites was formed.[32−34]

The electrochemical reaction in FeO_xF_{2-x} differs from that in FeF_2, wherein conversion is initiated at the surface and then gradually propagates into the bulk.[8] The early intercalation (>2.0 V) prior to the conversion reaction may offer a facile pathway for Li transport. The surface O-rich layer is believed to be sustained once it transforms into the rocksalt structure. The Li storage/release reaction in the rocksalt phase occurs reversibly (see Supporting Information, Figures S14 and S15), without destroying the particle morphology. As shown in Figure 1d, cycling stability would be enhanced significantly by the presence of this stable surface layer (as being verified by the measured performance in Figure 1d). There is also other beneficial impact of O substitution on the cycling stability of the electrodes. For example, the improved electronic conductivity of the O-rich oxyfluoride at the surface is expected to maintain a facile electron supply to the particle during cycling and so enhance electrochemical activity.[15] In addition, the disordered nature of the formed lithiated and delithiated phases (as examined by electron diffraction; Supporting Information, Figure S5) is also advantageous to improve the cycling stability. For the practical use as the cathode, lithium-containing electrodes may be made from nanocomposites of Li-containing species (*e.g.*, LiF) and Fe−O−F compounds, using a similar method as demonstrated in FeF_2/LiF electrodes.[35] It is expected that the electrochemical properties of the nanocomposite cathodes can be tuned by controlling the stoichiometry of the Fe−O−F compounds.

CONCLUSION

In this work, the STEM-EELS spectrum-imaging combined with magnetic measurements has been applied for studying local structural/chemical ordering in $FeO_{0.7}F_{1.3}$ nanoparticles during the first cycle, providing new insights into the impact of mixed anions on the electrochemical reaction process. Due to heterogeneity in the structure, with an F-rich core and an O-rich shell, the conversion reaction preferentially occurs at the core, while a rocksalt phase is formed predominantly at the surface. In the fully lithiated electrodes, the formation of percolating network of Fe^0 and rocksalt phase Li−Fe−O(−F) with high lattice coherency between the two may facilitate the electronic and ionic transport required for delithiation that leads to the rutile phase at the core and rocksalt at the shell. The relatively stable O-rich shell may prevent the direct interaction of the electrochemically active core with electrolyte, thereby enabling the mechanical and chemical stability of FeO_xF_{2-x} electrodes. Our finding, of encapsulating

the conversion compounds with stable surface layer, may offer a new strategy of developing high-energy, long-lasting conversion electrodes for lithium batteries.

EXPERIMENTAL SECTION

Synthesis and Electrochemical Cycling Test. $FeO_{0.7}F_{1.3}$ was prepared by heat treatment of synthesized $FeSiF_6 \cdot 6H_2O$ in ambient air, as reported previously.[13] For the test of the electrochemical cycling performance, electrodes were fabricated with 57.2 wt % active nanocomposite (ball-milled with 15 wt % activated carbon for 1h in He), 12.2 wt % carbon additive (SP, MMM), 30.5 wt % binder (2801, Alf Atochem) and plasticizer dibutyl phtalate (Aldrich) in acetone. CR-2320 coin cells (Hohsen) were assembled with lithium metal using glass-fiber separator embedded in 1 M $LiPF_6$ in ethylene carbonate (EC)/dimethyl carbonate (DMC) 50:50 in vol %. The cells were cycled between 1.5 and 4.5 V at 50 mA g^{-1} at 60 °C.

STEM-EELS Measurements. For STEM-EELS investigation, powder-based electrodes (1:1 mixture (in weight) of $FeO_{0.7}F_{1.3}$ and super-P carbon black with no binder), without further treatment, were used to sustain particle morphology. The assembled coin cells were cycled at 10 mA g^{-1} at room temperature. The coin cells were disassembled in the Ar-filled glovebox and the electrodes were rinsed thoroughly using DMC solvent and then transferred on to the TEM grids. The grids were then loaded onto a TEM holder inside the glovebox, and sealed in an Ar bag to protect the samples during the transportation to the TEM room. The samples were transferred to the TEM column within a few seconds, to minimize their exposure to the air.

Annular-dark-field (ADF) images were collected from an analytical TEM (JEOL 2100F) equipped with an ADF detector (Gatan 806). An aberration-corrected STEM (Hitachi HD 2700C) with a parallel EELS detector (Gatan Enfina-ER) was used to obtain high-resolution ADF images (spatial resolution of 1 Å) and EELS data (with an energy resolution of 0.35 eV). The STEM-EELS element mapping was collected at a collection angle of 26.7 mrad and a dispersion of 1.25 eV per channel. Both TEMs were operated at 200 kV. The possible electron beam damage was tested and addressed for each samples, and measurement condition was carefully optimized to minimize the radiation damage (Supporting Information, S1).

Magnetic Characterization. The magnetic measurements were performed on electrodes cycled to different stages. The electrode preparation and cycling conditions were similar to those described earlier.[7] The cells were disassembled in the glovebox, the retrieved electrodes were washed in DMC and dried under vacuum, and the active materials were scraped into plastic capsules sealed with vacuum grease to prevent air exposure. A SQUID magnetometer (Quantum Design MPMS XL-5) was employed to investigate the magnetic properties using the following protocols. First, the remnant magnetic field was quenched to less than 3 mOe using the ultralow field option, the sample was cooled to 2 K, and at that temperature, the magnetic field of 10 Oe was applied. Zero-field-cooled magnetization was measured while heating the sample from 2 to 400 K, followed by field-cooled magnetization measurements in the same field upon cooling of the sample from 400 to 2 K. Magnetization curves were measured at 2 and 298 K in magnetic fields up to 5 T. The sample was zero-field-cooled before the magnetization data at 2 K was taken. For the completely lithiated sample, two additional tests were performed: AC magnetic susceptibility was measured from 2 to 400 K after zero-field cooling, AC fields of 4 Oe with frequencies from 10 to 10 000 Oe were used, and also, the magnetization curves were measured at 2, 50, 100, 150, 200, 250, and 300 K in magnetic fields up to 9 T using Quantum Design PPMS.

XRD/XAS Characterization. The synchrotron XRD data from as-synthesized $FeO_{0.7}F_{1.3}$ were collected at beamline X14A of the National Synchrotron Light Source (NSLS) by a linear position-sensitive silicon detector (λ = 0.7747 Å). The XAS data (Fe K-edge) were collected at beamline X18A, NSLS. The measurements were performed in transmission mode using a Si (111) double-crystal monochromator. Energy calibration for the absorption edge was made using Fe foil as a reference (Fe K-edge: 7112 eV).

Conflict of Interest: The authors declare no competing financial interest.

Supporting Information Available: The Supporting Information is available free of charge on the ACS Publications website at DOI: 10.1021/acsnano.5b03643.

Electron beam damage control, HRTEM of pristine samples, STEM-ADF images showing the areas for the mapping, O/O + F ratio mapping, electron diffraction pattern (along with intensity profile), magnetization measurements, EELS quantitative analysis, high-resolution ADF images from different locations, crystal structure of the rocksalt $LiFeO_2$ and BCC-Fe^0, STEM-EELS mapping of the lithium and Fe (PDF)

Acknowledgment. We thank John Johnson, Lihua Zhang for technical support, and Tiffany Bowman for the graphic design (in TOC). The work was supported as part of the NorthEast Center for Chemical Energy Storage, an Energy Frontier Research Center funded by the U.S. Department of Energy, Office of Science, under Award Numbers DE-SC0001294 and DE-SC0012583. P.G. was grateful for the support by the U.S. Department of Energy, Office of Basic Energy Sciences, under Contract No. DE-SC0012704, with funding from Laboratory Directly Research and Development at Brookhaven. F.W. was grateful for the partial support by the U.S. Department of Energy (DOE) Office of Energy Efficiency and Renewable Energy under the Advanced Battery Materials Research (BMR) program, Contract No. DE-SC0012704. S.-W.K. was grateful for the partial support from the National Research Foundation (NRF) grant funded by the Korea Government (MSIP) (2012M2A8A5025697). Electron Microscopy work carried out at the Center for Functional Nanomaterials, and National Synchrotron Light Source, Brookhaven National Laboratory, were supported by the U.S. Department of Energy, Office of Basic Energy Sciences, under Contract No. DE-SC0012704.

REFERENCES AND NOTES

1. Badway, F.; Pereira, N.; Cosandey, F.; Amatucci, G. G. Carbon-Metal Fluoride Nanocomposites Structure and Electrochemistry of FeF_3: C. *J. Electrochem. Soc.* **2003**, *150*, A1209–A1218.
2. Poizot, P.; Laruelle, S.; Grugeon, S.; Dupont, L.; Tarascon, J. M. Nano-Sized Transition-Metal Oxides as Negative-Electrode Materials for Lithium-Ion Batteries. *Nature* **2000**, *407*, 496–499.
3. Malini, R.; Uma, U.; Sheela, T.; Ganesan, M.; Renganathan, N. G. Conversion Reactions: A New Pathway to Realise Energy in Lithium-Ion Battery — Review. *Ionics* **2009**, *15*, 301–307.
4. Cabana, J.; Monconduit, L.; Larcher, D.; Palacin, M. R. Beyond Intercalation Based Li Ion Batteries: The State of the Art and Challenges of Electrode Materials Reacting through Conversion Reactions. *Adv. Mater.* **2010**, *22*, E170–E192.
5. Amatucci, G. G.; Pereira, N. Fluoride Based Electrode Materials for Advanced Energy Storage Devices. *J. Fluorine Chem.* **2007**, *128*, 243–262.
6. Li, H.; Balaya, P.; Maier, J. Li-Storage *via* Heterogeneous Reaction in Selected Binary Metal Fluorides and Oxides. *J. Electrochem. Soc.* **2004**, *151*, A1878–A1885.
7. Wang, F.; Robert, R.; Chernova, N. A.; Pereira, N.; Omenya, F.; Badway, F.; Hua, X.; Ruotolo, M.; Zhang, R.; Wu, L.; Volkov, V.; Su, D.; Key, B.; Whittingham, M. S.; Grey, C. P.; Amatucci,

G. G.; Zhu, Y.; Graetz, J. Conversion Reaction Mechanisms in Lithium Ion Batteries: Study of the Binary Metal Fluoride Electrodes. *J. Am. Chem. Soc.* **2011**, *133*, 18828–18836.
8. Wang, F.; Yu, H. C.; Chen, M. H.; Wu, L.; Pereira, N.; Thornton, K.; Van der Ven, A.; Zhu, Y.; Amatucci, G. G.; Graetz, J. Tracking Lithium Transport and Electrochemical Reactions in Nanoparticles. *Nat. Commun.* **2012**, *3*, 1201.
9. Kim, S. W.; Seo, D. H.; Gwon, H.; Kim, J.; Kang, K. Fabrication of FeF_3 Nanoflowers on CNT Branches and Their Application to High Power Lithium Rechargeable Batteries. *Adv. Mater.* **2010**, *22*, 5260–5264.
10. Parkinson, M. F.; Ko, J. K.; Halajko, A.; Sanghvi, S.; Amatucci, G. G. Effect of Vertically Structured Porosity on Electrochemical Performance of FeF_2 Films for Lithium Batteries. *Electrochim. Acta* **2014**, *125*, 71–82.
11. Hua, X.; Robert, R.; Du, L. S.; Wiaderek, K. M.; Leskes, M.; Chapman, K. W.; Chupas, P. J.; Grey, C. P. Comprehensive Study of the CuF_2 Conversion Reaction Mechanism in a Lithium Ion Battery. *J. Phys. Chem. C* **2014**, *118*, 15169–15184.
12. Wang, F.; Kim, S. W.; Seo, D. H.; Kang, K.; Wang, L.; Su, D.; Vajo, J. J.; Wang, J.; Graetz, J. Ternary Metal Fluorides as High-Energy Cathodes with Low Cycling Hysteresis. *Nat. Commun.* **2015**, *6*, 6668.
13. Pereira, N.; Badway, F.; Wartelsky, M.; Gunn, S.; Amatucci, G. G. Iron Oxyfluorides as High Capacity Cathode Materials for Lithium Batteries. *J. Electrochem. Soc.* **2009**, *156*, A407–A416.
14. Bervas, M.; Klein, L. C.; Amatucci, G. G. Reversible Conversion Reactions with Lithium in Bismuth Oxyfluoride Nanocomposites. *J. Electrochem. Soc.* **2006**, *153*, A159–A170.
15. Chevrier, V. L.; Hautier, G.; Ong, S. P.; Doe, R. E.; Ceder, G. First-Principles Study of Iron Oxyfluorides and Lithiation of FeOF. *Phys. Rev. B: Condens. Matter Mater. Phys.* **2013**, *87*, 094118.
16. Kitajou, A.; Komatsu, H.; Nagano, R.; Okada, S. Synthesis of FeOF Using Roll-Quenching Method and the Cathode Properties for Lithium-Ion Battery. *J. Power Sources* **2013**, *243*, 494–498.
17. Wiaderek, K. M.; Borkiewicz, O. J.; Castillo-Martínez, E.; Robers, R.; Pereira, N.; Amatucci, G. G.; Grey, C. P.; Chupas, P. J.; Chapman, K. W. Comprehensive Insights into the Structural and Chemical Changes in Mixed-Anion FeOF Electrodes by Using Operando PDF and NMR Spectroscopy. *J. Am. Chem. Soc.* **2013**, *135*, 4070.
18. Ko, J. K.; Wiaderek, K. M.; Pereira, N.; Kinnibrugh, T. L.; Kim, J. R.; Chupas, P. J.; Chapman, K. W.; Amatucci, G. G. Transport, Phase Reactions, and Hysteresis of Iron Fluoride and Oxyfluoride Conversion Electrode Materials for Lithium Batteries. *ACS Appl. Mater. Interfaces* **2014**, *6*, 10858–10869.
19. Cosandey, F.; Su, D.; Sina, M.; Pereira, N.; Amatucci, G. G. Fe Valence Determination and Li Elemental Distribution in Lithiated $FeO_{0.7}F_{1.3}$/C Nanocomposite Battery Materials by Electron Energy Loss Spectroscopy (EELS). *Micron* **2012**, *43*, 22–29.
20. Sina, M.; Nam, K.-W.; Su, D.; Pereira, N.; Yang, X.-Q.; Amatucci, G. G.; Cosandey, F. Structural Phase Transformation and Fe Valence Evolution in FeO_xF_{2-x}/C Nanocomposite Electrodes during Lithiation and De-lithiation Processes. *J. Mater. Chem. A* **2013**, *1*, 11629–11640.
21. Chernova, N. A.; Nolis, G. M.; Omenya, F. O.; Zhou, H.; Li, Z.; Whittingham, M. S. What Can We Learn about Battery Materials from Their Magnetic Properties? *J. Mater. Chem.* **2011**, *21*, 9865–9875.
22. Stout, J. W.; Catalano, E. Heat Capacity and Entropy of FeF_2 and CoF_2 from 11 to 300 K. Thermal Anomalies Associated with Antiferromagnetic Ordering. *J. Chem. Phys.* **1955**, *23*, 1803–1808.
23. Kumar, D.; Narayan, J.; Kvit, A. V.; Sharma, A. K.; Sankar, J. High Coercivity and Superparamagnetic Behavior of Nanocrystalline Iron Particles in Alumina Matrix. *J. Magn. Magn. Mater.* **2001**, *232*, 161–167.
24. Su, D.; Wang, F.; Ma, C.; Jiang, N. Engineering Nano-Composite $Li_4Ti_5O_{12}$ Anodes *via* Scanning Electron-Probe Fabrication. *Nano Energy* **2013**, *2*, 343–350.
25. Wang, F.; Graetz, J.; Moreno, M. S.; Ma, C.; Wu, L.; Volkov, V.; Zhu, Y. Chemical Distribution and Bonding of Lithium in Intercalated Graphite: Identification with Optimized Electron Energy Loss Spectroscopy. *ACS Nano* **2011**, *5*, 1190–1197.
26. Fonseca, F. C.; Goya, G. F.; Jardim, R. F.; Mucillo, R.; Carreon, N. L. V.; Longo, E.; Leite, E. R. Superparamagnetism and Magnetic Properties of Ni Nanoparticles Embedded in SiO_2. *Phys. Rev. B: Condens. Matter Mater. Phys.* **2002**, *66*, 104406.
27. Colliex, C.; Manoubi, T.; Ortiz, C. Electron-Energy-Loss-Spectroscopy Near-Edge Fine Structures in the Iron-Oxygen System. *Phys. Rev. B: Condens. Matter Mater. Phys.* **1991**, *44*, 11402.
28. Riedl, T.; Gemming, T.; Wetzig, K. Extraction of EELS White-Line Intensities of Manganese Compounds: Methods, Accuracy, and Valence Sensitivity. *Ultramicroscopy* **2006**, *106*, 284–291.
29. Van Aken, P. A.; Liebscher, B. Quantification of Ferrous/Ferric Ratios in Minerals: New Evaluation Schemes of Fe L_{23} Electron Energy-Loss Near-Edge Spectra. *Phys. Chem. Miner.* **2002**, *29*, 188–200.
30. Li, L.; Meng, F.; Jin, S. High-Capacity Lithium-Ion Battery Conversion Cathodes Based on Iron Fluoride Nanowires and Insights into the Conversion Mechanism. *Nano Lett.* **2012**, *12*, 6030–6037.
31. Gmitter, A. J.; Badway, F.; Rangan, S.; Bartynski, R. A.; Halajko, A.; Pereira, N.; Amatucci, G. G. Formation, Dynamics, and Implication of Solid Electrolyte Interphase in High Voltage Reversible Conversion Fluoride Nanocomposites. *J. Mater. Chem.* **2010**, *20*, 4149–4161.
32. Zhang, W.; Ma, L.; Yue, H.; Yang, Y. Synthesis and Characterization of *In Situ* Fe_2O_3-Coated FeF_3 Cathode Materials for Rechargeable Lithium Batteries. *J. Mater. Chem.* **2012**, *22*, 24769–24775.
33. Zhou, H.; Nanda, J.; Martha, S. K.; Adcock, J.; Idrobo, J. C.; Baggetto, L.; Gabriel, M. V.; Dai, S.; Sreekanth, P.; Dudney, N. J. Formation of Iron Oxyfluoride Phase on the Surface of Nano-Fe_3O_4 Conversion Compound for Electrochemical Energy Storage. *J. Phys. Chem. Lett.* **2013**, *4*, 3798–3805.
34. Zhou, H.; Ruther, R. E.; Adcock, J.; Zhou, W.; Dai, S.; Nanda, J. Controlled Formation of Mixed Nanoscale Domains of High Capacity Fe_2O_3–FeF_3 Conversion Compounds by Direct Fluorination. *ACS Nano* **2015**, *9*, 2530–2539.
35. Kim, S. W.; Nam, K. W.; Seo, D. H.; Hong, J.; Kim, H.; Gwon, H.; Kang, K. Energy Storage in Composites of a Redox Couple Host and a Lithium Ion Host. *Nano Today* **2012**, *7*, 168–173.